AIAA JOURNAL
Vol. 43, No. 2, February 2005

Penetration of a Transverse Supersonic Jet into a Subsonic Compressible Crossflow

Steven J. Beresh,* John F. Henfling,† Rocky J. Erven,‡ and Russell W. Spillers§
Sandia National Laboratories, Albuquerque, New Mexico 87185

Particle image velocimetry data have been acquired in the far field of the interaction generated by an overexpanded axisymmetric supersonic jet exhausting transversely from a flat plate into a subsonic compressible crossflow. Mean velocity fields were found in the streamwise plane along the flowfield centerline for different values of the crossflow Mach number M_∞ and the jet-to-freestream dynamic pressure ratio J. The magnitude of the streamwise velocity deficit and the vertical velocity component both decay with downstream distance and were observed to be greater for larger J while M_∞ remained constant. Jet trajectories derived independently using the maxima of each of these two velocity components are not identical, but show increasing jet penetration for larger J. Similarity in the normalized velocity field was found for constant J at two different transonic M_∞, but at two lower M_∞ the jet appeared to interact with the wall boundary layer and data did not collapse. The magnitude and width of the peak in the vertical velocity component both increase with J, suggesting that the strength and size of the counter-rotating vortex pair increase and, thus, may have a stronger influence on aerodynamic surfaces despite further jet penetration from the wall.

Introduction

ATMOSPHERIC flight vehicles that employ supersonic jets for attitude or roll control may find their expected performance altered due to interactions concerning the exhausting jet. The aerodynamic interaction of the jet with the crossflowing freestream will modify the pressure distribution on the surface of the vehicle, creating an additional force that can either amplify or detract from the thrust of the jet itself.[1−7] Furthermore, this freestream interaction causes the jet to turn following exit from the nozzle and travel downstream, where it can interact with aerodynamic control surfaces, such as fins found on bombs or missiles. Past studies have indicated that this jet/fin interaction can change the pressure field on the fins and, hence, the force they generate,[3,5,7−10] which may yield effects deleterious to the performance of the vehicle.

To predict the effects of the jet/fin interaction, it is necessary to understand the trajectory and spreading of the jet, which itself is determined by the jet-in-crossflow interaction with the freestream. Figure 1 shows the common features of a jet-in-crossflow interaction as found by past studies.[1,11−16] The far field of the interaction is dominated by the presence of a counter-rotating vortex pair, induced as the jet is turned over and realigned by its encounter with the freestream. These strong vortices are believed to be principally responsible for the interaction with downstream fins and, hence, merit the focus of an investigation that seeks to explore the nature of jet/fin interaction.

The present study experimentally examines the interaction generated by a supersonic jet exhausting transversely from a flat plate into a subsonic compressible crossflow, with its principal focus on the detection of the jet trajectory and the induced vortex pair. Particle image velocimetry (PIV) was conducted in a streamwise plane of the far field of the jet-in-crossflow interaction to determine the streamwise and vertical velocity components, providing an inference of the size and location of the vortex pair and the strength of the generated vorticity. Data were collected for a variety of flowfield conditions to examine the impact of varying the jet-to-freestream dynamic pressure ratio and the freestream Mach number, which previously have been identified as key similarity parameters.[1,17−20]

Whereas similar velocimetry studies have been conducted for transverse jets in low-speed flows,[18,20−25] such work is less common for compressible flows. Previous velocimetry measurements of a jet exhausting into a supersonic crossflow have been made using laser Doppler velocimetry for a transverse sonic jet,[26] hot-film anemometry for an angled supersonic jet,[27] and PIV of a jet issuing from a missile half-body.[28] Other approaches to measuring jet penetration into a supersonic flow have included schlieren photography,[19] concentration measurements of differing fluids,[17,29] Mie scattering (see Refs. 30 and 31), and laser-induced fluorescence.[32] The current efforts, therefore, build upon such previous work by providing high-fidelity PIV data for a compressible jet in crossflow, and additionally fill a gap by examining the transonic flow regime, for which jet penetration measurements appear limited to pressure-probe investigations.[33,34] These quantitative data are ideal for the validation of computational simulations and the evolution of their underlying physical models. Furthermore, the present study yields velocimetry data for flowfield conditions that are particularly relevant toward understanding jet/fin interaction found on atmospheric finned vehicles.

Experimental Apparatus

Trisonic Wind Tunnel

All experiments were performed in the Sandia National Laboratories Trisonic Wind Tunnel (TWT). The TWT is a blowdown-to-atmosphere facility with interchangeable test sections, each using air as the test gas. One is a transonic nozzle permitting a continuously variable Mach number from 0.5 to 1.3. The 305×305 mm^2 (12×12 in.^{2}) rectangular test section traditionally has been fitted with porous walls and is enclosed in a pressurized plenum to contain the flow that passes through them, but in the present case the porous walls have been replaced with solid walls. This serves both to supply a flat plate from which the jet will issue and to provide computationally tractable boundary conditions for comparison of experimental data and numerical simulations. Use of a wall-mounted jet was deemed superior to a sting-mounted flat plate to avoid such uncertainties as plate deflection and flow interference from the jet

Presented as Paper 2004-1112 at the 42nd Aerospace Sciences Meeting, Reno, NV, 5–8 January 2004; received 8 April 2004; revision received 23 August 2004; accepted for publication 23 August 2004.

*Senior Member Technical Staff, Engineering Sciences Center, P.O. Box 5800, Mailstop 0834; sjberes@sandia.gov. Senior Member AIAA.
†Distinguished Technologist, Engineering Sciences Center.
‡Senior Technologist, Engineering Sciences Center.
§Technologist, Engineering Sciences Center.

supply apparatus beneath the plate. The use of a solid-wall test section limits the Mach number range of the flowfield, but this was considered an acceptable compromise.

Supersonic Jet Hardware

The jet exhausted from a conical nozzle with a design Mach number of 3.73, an expansion half-angle of 15 deg, and an exit diameter of 9.53 mm (0.375 in.). The nozzle is fit to a settling chamber designed for a maximum pressure of 14 MPa (2000 psia) and instrumented with a transducer and a thermocouple to provide stagnation pressure and temperature measurements. A manifold of six nitrogen bottles pressurized to 24 MPa (3500 psi) provided the gas source for the nozzles.

The nozzle mounts along the centerline of the top wall of the test section, which served as the flat plate from which it transversely exhausted. A side-wall window lies flush with the top wall and is positioned downstream of the jet for viewing the far field of the interaction; a larger window in the pressurized plenum complements the test section window. A window in the floor of the test section is located near the position of the side-wall window for introducing the laser sheet, which is matched by a second laser window in the bottom of the plenum. The relative position of the jet and windows within the test section is shown in Fig. 2. Figure 2 additionally shows the laser sheet for the PIV measurements and a pressure tap contained in each side wall for measuring the static pressure in the test section to determine the freestream Mach number.

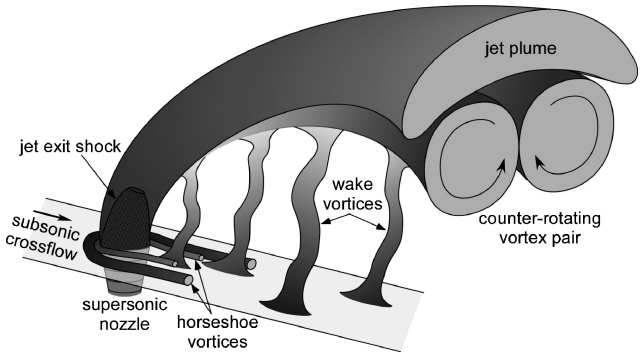

Fig. 1 Common features of jet-in-crossflow interaction.

PIV System

PIV measurements presented in the current study are two dimensional, acquired with the laser sheet aligned in the streamwise direction of the wind tunnel positioned downstream of the jet nozzle on the test section centerline, as shown in Fig. 2. The plane in which the laser sheet lies passes through the centerline axis of the jet nozzle. The coordinate system is chosen such that the u component lies in the streamwise direction and the v component is in the vertical direction, positive away from the top wall. The origin is located at the center point of the jet nozzle exit plane.

The light source of the system is a pair of frequency-doubled Nd:YAG lasers (Coherent Infinity Model 40-100) that can operate with a variable repetition rate but in the present study are used exclusively at 15 Hz producing about 100 mJ/beam. The beams are combined such that both maintain the same polarization then are formed into coplanar sheets beneath the wind tunnel and directed into the test section, where the sheet thickness is 1.2 mm (0.048 in.). The pulse separation time is monitored by a photodiode read by a fast oscilloscope and was found to be $2.375 \pm 0.005\ \mu$s. Synchronization with the camera is accomplished using two digital delay generators (Stanford Research Systems Model DG535).

Scattered light is collected by a frame-straddling charge-coupled device camera (Redlake MegaPlus Model ES4.0/E), which allows the exposure associated with each laser pulse to be stored independently. This camera has a resolution of 2048×2048 pixels, digitizes at 8 bit, and can acquire pairs of images at about 7 Hz. The camera was equipped with a 105-mm lens (Nikon Micro-Nikkor) operating at $f/4$ and imaged a field of view measuring approximately 160×160 mm^2 (6.2×6.2 in.^{2}). The camera stood 1.1 m from the laser sheet. Given that the angle subtended by the scattered light and the camera axis is small, and that the flowfield is dominated by the streamwise velocity component, perspective error due to the collection angle of the camera lens is expected to be minor.[35,36]

The flowfield was surveyed using two separate imaging regions, as indicated in Fig. 2, so that a greater streamwise distance of the interaction could be measured. A single camera was used, which was relocated to a downstream position for a separate set of wind-tunnel runs. The streamwise laser sheet location was altered as well to maximize its downstream projection. The farthest upstream edge of the combined imaging region was constrained by the side-wall window through which the camera looked, whereas the farthest downstream edge was limited by the laser sheet position. An overlap between the

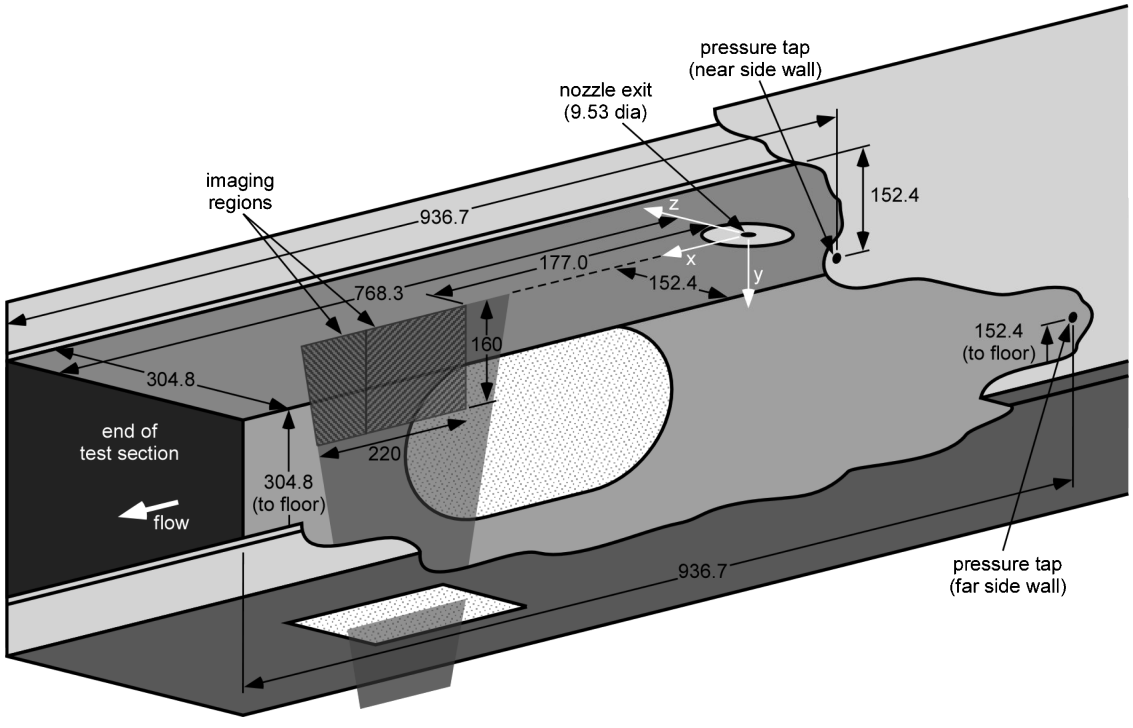

Fig. 2 Schematic (not to scale) of jet-in-crossflow configuration in TWT for PIV measurements; flow from right to left, dimensions in millimeters.

two stations ensured complete coverage of the resulting trapezoidal imaging region and also permitted a comparison between measurements at each position for uncertainty assessment, discussed later.

The TWT is seeded by a thermal smoke generator (Corona Vi-Count Model 5000) that produces a large quantity of particles specified by the manufacturer as 0.2–0.3 μm in diameter from a mineral oil base. The smoke generator is contained within a pressurized tank to force the smoke through a duct into the elevated pressure of the TWT's stagnation chamber, where injector tubes distribute the particles through a portion of the flow that will eventually reach the region of interest within the test section. The flow conditioning section of the TWT removes disturbances induced by particle injection and assists in dispersing the particles. The jet itself remains unseeded. Although this creates a serious measurement bias near the jet exit due to selective flow sampling, data acquired farther downstream are not subject to such a difficulty because turbulent mixing entrains particles from the freestream and spreads them throughout the interaction once in the far field. The particles are sufficiently small that they will rapidly attain the local velocity once they have been redistributed.[37,38] Thus, images acquired farther downstream are properly seeded, and velocity measurements are no longer subject to a bias from having used particles that originate exclusively in the freestream.

As a result of the seeding density necessary to produce sufficient intensity of the side-scattered light, and because the diffraction-limited particle image size is about 5–10 μm in diameter, whereas an individual pixel in the camera covers about an 80-μm length, multiple particle images are commonly found at any given pixel. Therefore, speckle effects from interactions in the scattered light produce patterns in the image rather than distinct particles. This is not, however, an impediment to successful PIV measurements; unique speckle patterns may be correlated between the two PIV exposures. This produces somewhat noisier results than those from discretely resolved particle images.[39,40]

PIV data have been processed using IDT's ProVision 2.02 software. Vectors are produced using a 64×64 pixel interrogation window with a 50% overlap, yielding a $5.0 \times 5.0\,\text{mm}^2$ ($0.20 \times 0.20\,\text{in.}^2$) spatial resolution. A streamwise window offset is established between the two exposures corresponding to the freestream convection distance expected from the given time between laser pulses, which has been shown to improve the accuracy of cross-correlation analysis.[41] Resulting vector fields are validated based on signal-to-noise and nearest-neighbor criteria.

Experimental Conditions

The testing conditions have been selected to approximate those found on transonic flight vehicles that employ supersonic jets for attitude or roll control. The primary freestream Mach number is $M_\infty = 0.8$ with a wind-tunnel stagnation pressure $P_0 = 154$ kPa (22.4 psia), which yields a freestream static pressure $p_w = 101$ kPa (14.7 psia). The wind-tunnel unit Reynolds number at these conditions is 20×10^6 m^{-1} (6×10^6 ft^{-1}). The nominal stagnation pressure for the Mach 3.73 jet is $P_{0j} = 4.96$ MPa (720 psia), providing a perfectly expanded jet exit pressure of $p_e = 47.1$ kPa (6.84 psia). These conditions combine to produce a nominal jet-to-freestream dynamic pressure ratio $J = 10.2$. Additional cases were employed to span a range of J values while maintaining a constant $M_\infty = 0.8$, or to span a range of subsonic values of M_∞ while maintaining a constant $J = 10.2$. Table 1 lists the conditions for the seven cases studied. All cases were chosen such that $p_w = 101$ kPa (14.7 psia); therefore, the jet was always overexpanded. This wall pressure was measured from the mean of two static pressure taps located on the wind-tunnel side walls 168 mm upstream of the jet nozzle centerline, as seen in Fig. 2. M_∞ and the velocity reference U_∞ were calculated isentropically from the ratio p_w/P_0 and the stagnation temperature T_0. The choice of M_∞ and J must keep within the subsonic restrictions imposed by the tunnel blockage issues inevitable with the solid-wall transonic test section.

Table 1 Experimental conditions for the jet and wind tunnel

Case	J	M_∞	P_0, kPa	P_{0j}, MPa	U_∞, m/s
1	10.2	0.80	154	4.97	286
2	16.7	0.80	154	8.14	286
3	5.6	0.80	154	2.76	286
4	2.8	0.80	154	1.36	286
5	10.2	0.70	141	3.82	251
6	10.2	0.60	129	2.79	215
7	10.2	0.50	120	1.96	181

The gas supply for the jet is unheated, so that the jet stagnation temperature T_{0j} varied from 296 to 307 K (533 to 553°R) depending on the laboratory ambient conditions. The wind-tunnel air supply is heated in the storage tanks but not temperature controlled subsequent to this; therefore, the freestream stagnation temperature T_0 also is subject to slight variation and fluctuated from 324 to 329 K (582 to 591°R).

The 99%-velocity boundary-layer thickness has been determined from the present PIV data on the wind-tunnel top wall in the undisturbed test section, in which the jet nozzle has been replaced by a blank to preserve the flat wall. At the center of the upstream PIV imaging region, which is 254 mm downstream of the jet nozzle centerline, the data yield a value of 14.6 ± 0.9 mm ($1.53 \pm 0.1 d_j$).

The trapezoidal PIV imaging region stretches from 176 to 440 mm downstream of the jet nozzle centerline, or 18.5–46.2 jet diameters d_j, although the inclined laser sheet limits the horizontal edge to 400 mm ($42.0 d_j$) downstream at the edge farthest from the wall. For the nominal flow conditions (case 1 in Table 1), 15 wind-tunnel runs of 201 image pairs each were collected at the upstream imaging region and 9 wind tunnel runs of 201 image pairs at the downstream position. For the other six cases, five wind tunnel runs of 201 image pairs each were conducted for each camera position.

Results and Discussion

Velocity Fields

The PIV data collected for each of the seven flowfield cases were first validated as already described, then all valid vectors were collapsed into a mean velocity field representing that case. Because the imaging region is located in the far field of the jet interaction, the flow is dominated by the streamwise velocity component, and, hence, an examination of the data via a vector plot is of limited value. A more illuminating approach is to view each velocity component as a separate contour plot, which is done in Figs. 3 and 4 for each case. Figure 3 shows the streamwise velocity component u, and Fig. 4 shows the vertical velocity component v. Vertical distances in Figs. 3 and 4 are measured from the top wall of the wind tunnel where the jet nozzle is located, and horizontal distances are measured from the centerline of the jet nozzle. Distances are normalized to the jet exit diameter d_j and velocities to U_∞.

The first observation from Figs. 3 and 4 is that, as anticipated, the jet penetration and trajectory are readily discernable from the velocity field, as is the breadth of the jet's influence. The deficit in u seen in Fig. 3 tracks the position of the jet from its impedance of the oncoming crossflow, whereas the increase in v in Fig. 4 marks the location of the counter-rotating vortex pair due to the induced vertical velocity component. Whether observed using u or v, the jet and associated vortices can be seen to penetrate farther into the freestream for larger values of J while $M_\infty = 0.8$. The behavior is more complex when M_∞ is reduced while $J = 10.2$; the jet penetration appears the same for $M_\infty = 0.8$ and $M_\infty = 0.7$, but the jet seems to interact with the wall boundary layer at $M_\infty = 0.6$ and $M_\infty = 0.5$ as shown in Fig. 3. This behavior is discussed further later. It also is evident that the position of the maximum deficit in u does not coincide with the maximum in v.

Similarly, the decay of the jet and vortex strength is apparent in Figs. 3 and 4 by the decrease in the velocity deficit in u and vertical velocity v with downstream distance in each case. The deficit in u is greater for larger values of J, indicating the increased blockage of a stronger jet, and appears identical in Figs. 3a and 3e for $M_\infty = 0.8$ and $M_\infty = 0.7$, where J is constant. However, for the two lowest values of M_∞, the decay of u is more difficult to distinguish due to the apparent interaction with the boundary layer. The same trends are visible for the decay of the magnitude of v in Fig. 4, except that the

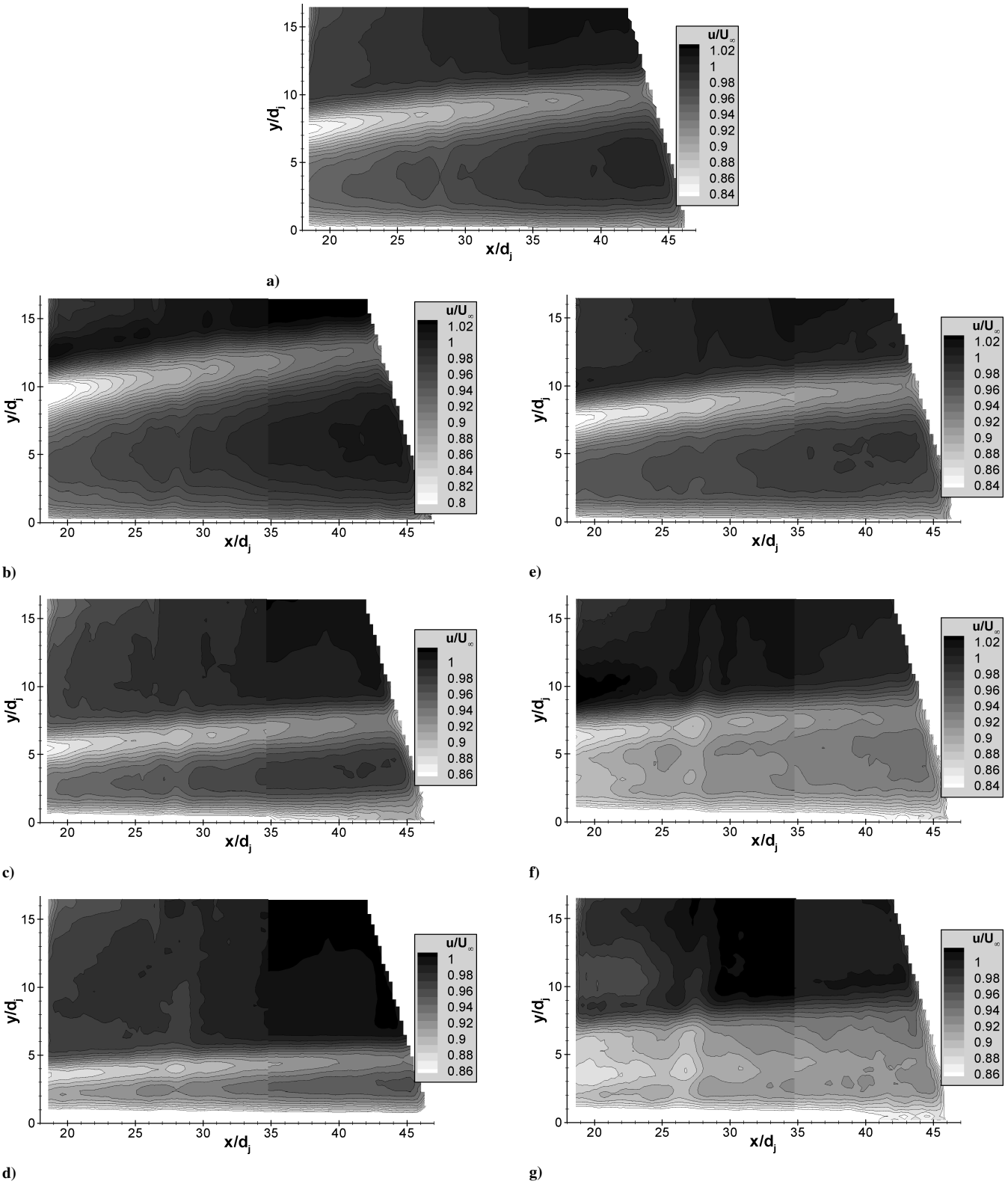

Fig. 3 Mean streamwise velocity component for jet-in-crossflow interaction: a) $J = 10.2$ and $M_\infty = 0.8$, b) $J = 16.7$ and $M_\infty = 0.8$, c) $J = 5.6$ and $M_\infty = 0.8$, d) $J = 2.8$ and $M_\infty = 0.8$, e) $J = 10.2$ and $M_\infty = 0.7$, f) $J = 10.2$ and $M_\infty = 0.6$, and g) $J = 10.2$ and $M_\infty = 0.5$.

presence of the vortices is more easily discerned for $M_\infty = 0.6$ and $M_\infty = 0.5$ than it was for u. The greater degree of noise for $M_\infty = 0.6$ and $M_\infty = 0.5$ is probably because the lower U_∞ reduces the signal-to-noise ratio of the measurement. Nevertheless, it is clear that the behavior of these two cases is dissimilar from that of $M_\infty = 0.8$ and $M_\infty = 0.7$ despite having matched values of J.

The gradual increase in freestream values of u in the streamwise direction visible for all seven cases in Fig. 3 is quite real. This arises because the wind-tunnel test section has a constant cross-sectional area. As the boundary layer grows with downstream distance, an increase is observed in the local Mach number and, hence, the streamwise velocity. This rise in the freestream u is greater for larger values of J and for $M_\infty = 0.8$ and $M_\infty = 0.7$ as compared to $M_\infty = 0.6$ and $M_\infty = 0.5$. Such behavior is consistent with greater jet penetration inducing more blockage into the flowfield and, hence, driving up the local Mach number as the flow accelerates around

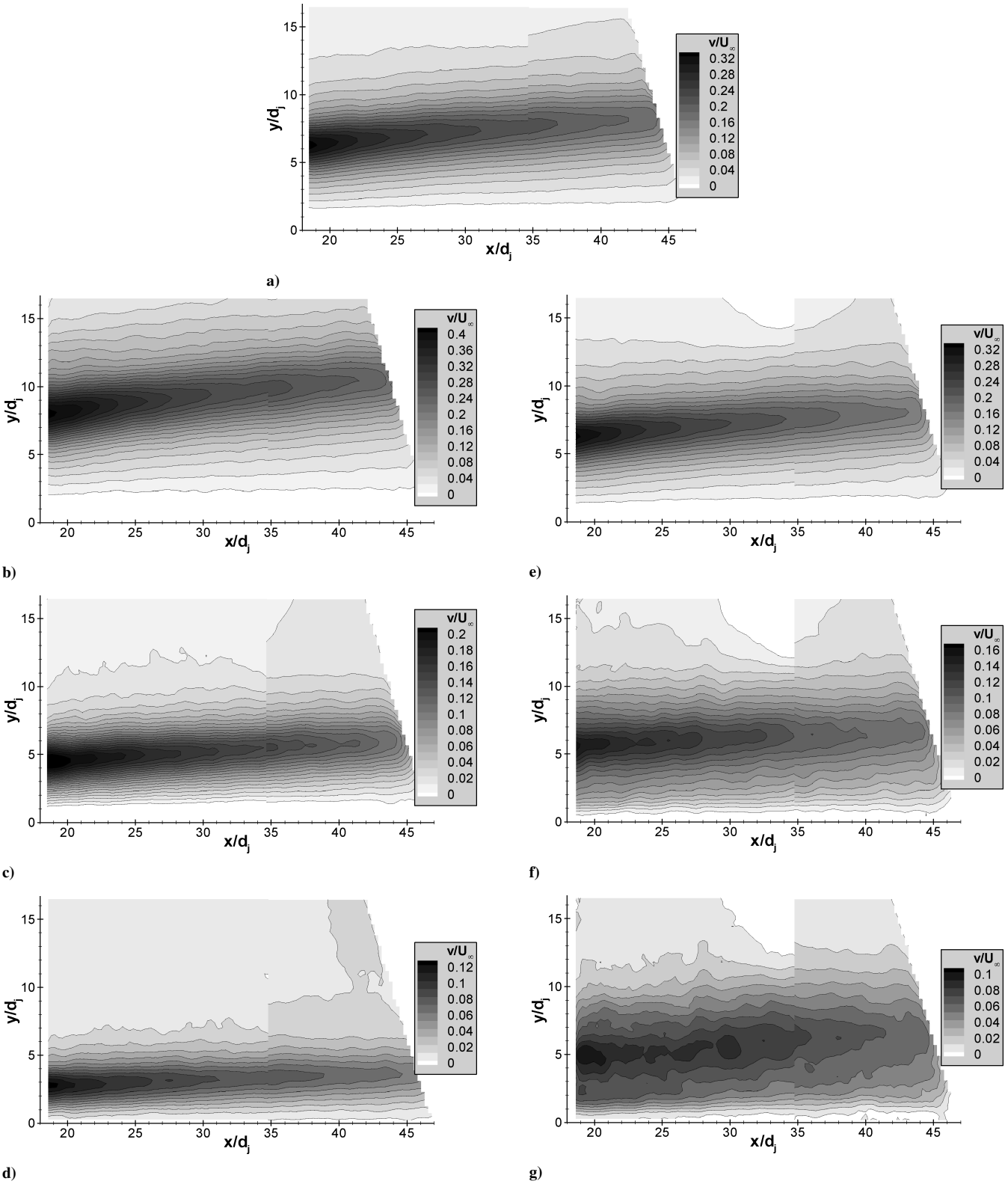

Fig. 4 Mean vertical velocity component for jet-in-crossflow interaction: a) $J = 10.2$ and $M_\infty = 0.8$, b) $J = 16.7$ and $M_\infty = 0.8$, c) $J = 5.6$ and $M_\infty = 0.8$, d) $J = 2.8$ and $M_\infty = 0.8$, e) $J = 10.2$ and $M_\infty = 0.7$, f) $J = 10.2$ and $M_\infty = 0.6$, and g) $J = 10.2$ and $M_\infty = 0.5$.

the jet interaction. Curiously, in each case $u/U_\infty = 1$ occurs near the middle of the PIV imaging region, which lies 30–35d_j downstream of the jet nozzle and, therefore, 48–53d_j downstream of the wall pressure taps at which M_∞ and U_∞ are calculated. Because both the wall boundary-layer growth and the jet blockage tend to increase U_∞ slowly but steadily as a function of downstream distance, $u/U_\infty = 1$ should occur at the pressure taps, which are well upstream of the PIV measurements. If the trends in the PIV data are extrapolated back to the pressure taps, the difference is estimated as 2–3% of U_∞ and suggests a measurement bias exists. PIV measurements in the undisturbed freestream, however, have been shown to agree with pitot probe measurements, implying that the error lies in U_∞. Wind-tunnel nonuniformities near the test section inlet may be responsible because the pressure taps lie on the side walls and the PIV freestream data are acquired near the test section centerline. This is particularly plausible given that the wind-tunnel contraction

section possesses different wall curvature on the horizontal planes compared with the vertical planes.

The streamwise velocities in the wake of the jet, that is, between the decaying jet and the wall, also increase with downstream distance as the flow recovers from the initial injection of the jet into the crossflow. Even while these wake velocities rise, they lag behind the local freestream velocity, indicating the continued presence of the wake effects of the jet. An exception to this observation is made for the cases where $M_\infty = 0.6$ and $M_\infty = 0.5$ because here the interaction between the jet and the boundary layer makes the concept of a jet wake unclear.

Note that for the streamwise velocities in Fig. 3, an artificial reduction in velocity can be observed in the upper-left-hand corner of each contour plot and along the inclined downstream edge of the measurement region. Both occurred near an edge of the laser sheet, and although vectors nearest these boundaries were removed, a more subtle influence evidently existed adjacent to the discarded vectors. Similarly, the vertical seams visible in Figs. 3 and 4 are an artifact of having combined data from two distinct camera positions; these incongruities lie within the uncertainty of the measurements.

Measurement uncertainties in the mean velocity data consist principally of biases in the PIV calibration, flowfield repeatability from one wind-tunnel run to another, and convergence of the mean. The data for the nominal flow conditions (case 1) were acquired over a number of days and, thus, employed multiple calibrations; all other cases were acquired in sequence using a single calibration. Therefore, the nominal case can be used to determine the uncertainty in the mean velocity data by computing the scatter between means found using different calibrations, then the resulting bias estimate may be applied to mean data acquired using any one calibration. This shows that the uncertainty estimate for the mean velocity data, defined as the 95% confidence interval, is a maximum of about ± 7 m/s within the jet interaction and falls to about ± 4 m/s in the freestream. The typical uncertainty in J is ± 0.1 and in M_∞ is ± 0.002, again determined as 95% confidence intervals. These run-to-run variations in the flowfield parameters are partly responsible for the mean velocity field uncertainties. With the exception of the $M_\infty = 0.6$ and $M_\infty = 0.5$ cases, calibration bias was found to exceed uncertainty due to repeatability and data convergence.

Additional wind-tunnel runs were conducted for the nominal case in which the time between laser pulses was steadily increased from the standard value of 2.375 μs to a maximum of 6.375 μs. Changing this parameter did not significantly alter the results, indicating that out-of-plane motion did not induce a bias error by selectively removing some particles from the PIV correlations.

Velocity Profiles

Data such as those shown in Figs. 3 and 4 can be viewed in a more quantitative format by extracting specific lines of velocity vectors from the PIV vector fields and plotting each component independently. Vertical lines of velocity data were extracted at 200, 250, 300, 350, and 400 mm downstream of the jet nozzle centerline (21.0, 26.2, 31.5, 36.7, and 42.0d_j downstream) and are shown in Figs. 5 and 6 for the streamwise and vertical components, respectively. In

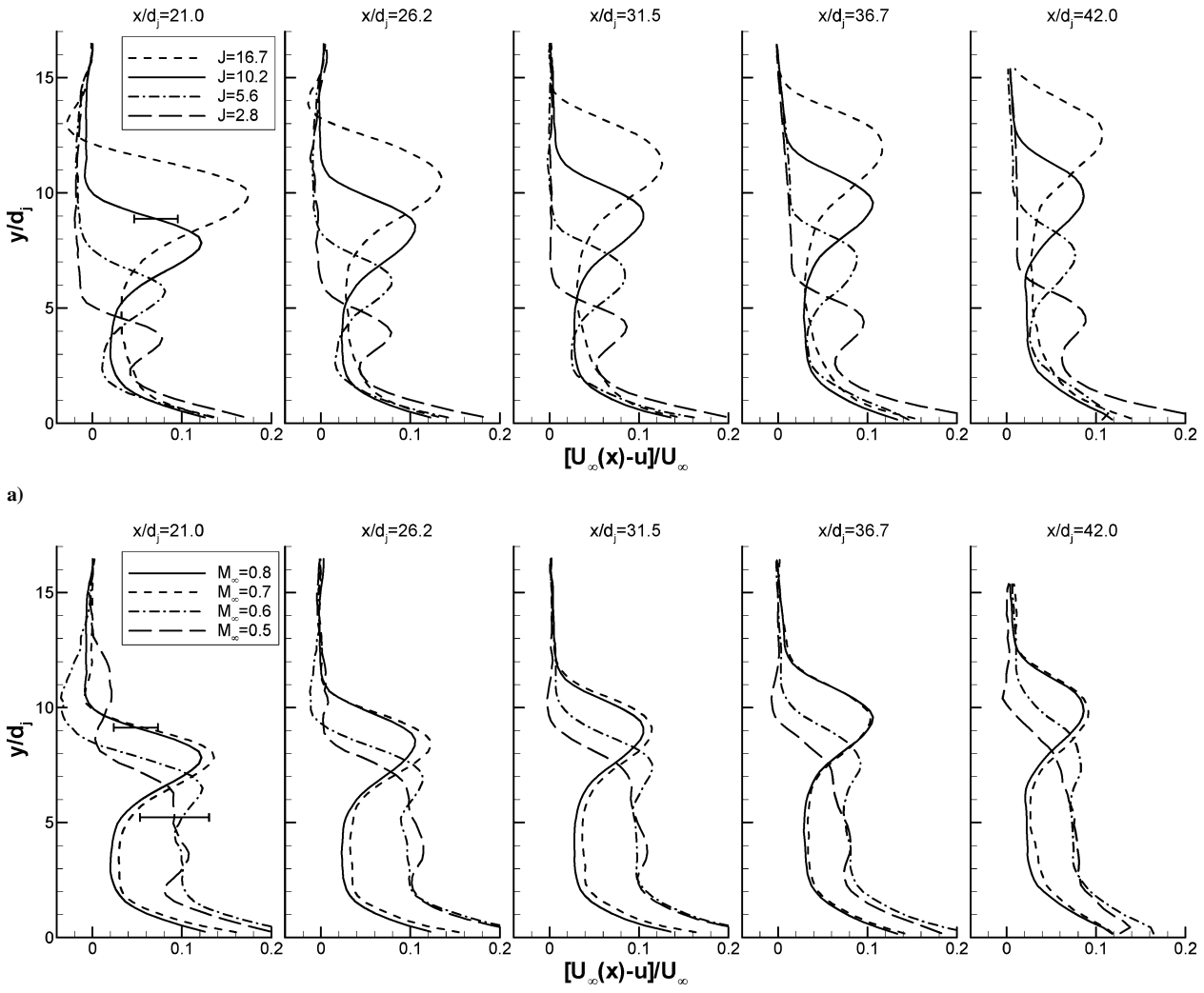

Fig. 5 Mean streamwise velocity deficit extracted from Fig. 3 at five locations downstream of the jet nozzle centerline: a) varying J while $M_\infty = 0.8$ and b) varying M_∞ while $J = 10.2$.

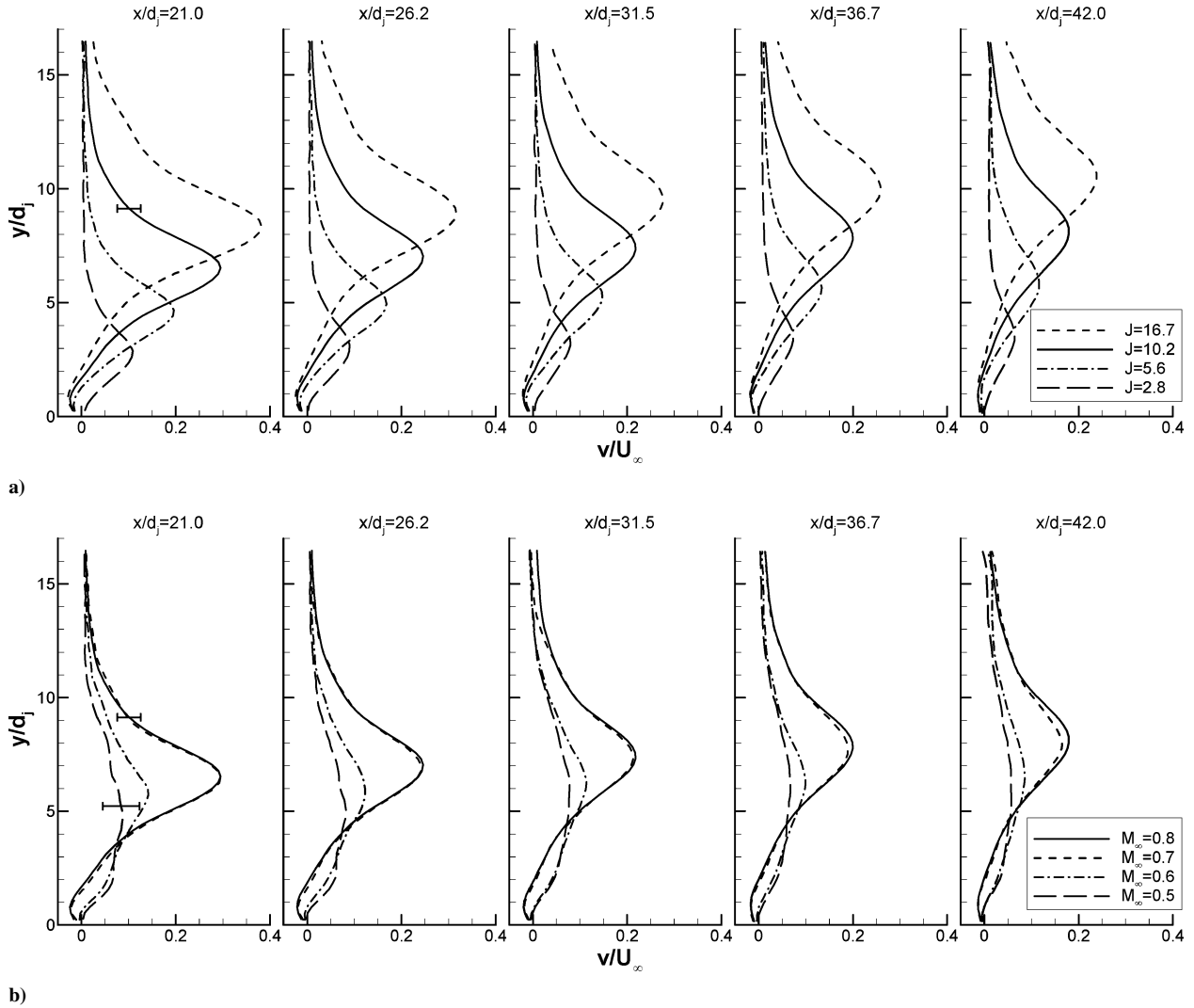

Fig. 6 Mean vertical velocity component extracted from Fig. 4 at five locations downstream of the jet nozzle centerline: a) varying J while $M_\infty = 0.8$ and b) varying M_∞ while $J = 10.2$.

Fig. 5, the streamwise component is represented as a velocity deficit $[U_\infty(x) - u]/U_\infty$, which thus removes the influence of the gradual increase in the freestream velocity by treating it as a local property. The value $U_\infty(x)$ is determined from the PIV data in the freestream to capture the increase in M_∞; conversely, U_∞ is found from the pressure taps and has no dependence on downstream distance. Sample error bars are shown in Figs. 5 and 6, which appear relatively large because the farfield velocities induced by the jet are a small fraction of the freestream velocity. The error bars for $M_\infty = 0.5$ in Figs. 5b and 6b are larger than those for $M_\infty = 0.8$ because a constant uncertainty in u or v becomes larger when normalized to a smaller U_∞ and because the statistical convergence of this case is poorer.

The trends found in Figs. 3 and 4 can be seen more distinctly in Figs. 5 and 6. The influence of J while M_∞ is held constant can be examined from Figs. 5a and 6a. A prominent velocity deficit is observed in u whose location moves farther away from the wall as J is increased. Similarly, v shows a profound increase associated with the presence of the counter-rotating vortex pair, whose position increases with J. The magnitude and width of the peak in v both increase with J, suggesting that as J becomes greater, the strength and size of the vortices increase even as they move further from the wall; this observation is consistent with previous studies.[3,42] The magnitude of the velocity deficit in u shows similar behavior, and a deficit persists even beneath the vortices due to the wake effect of the jet presence.

Trends as a function of M_∞ while J remains constant are more complex, however, as was first noticed in Figs. 3 and 4. Figures 5b and 6b show that, when $M_\infty = 0.8$ and $M_\infty = 0.7$, the normalized velocities collapse to a single profile, within the measurement uncertainty. The utility of J as a similarity parameter previously has been shown for both incompressible[1,18,20] and high-speed interactions.[17,19,30] Where $M_\infty = 0.6$ and $M_\infty = 0.5$, no such similarity is observed. The apparent interaction with the boundary layer for these two cases is evident in Fig. 5b, where the velocity deficit tends not to exhibit as distinct a peak and instead is maintained to the wall boundary layer. This contrasts with every other case in Fig. 5, in which a distinct jet wake is seen between the jet itself and the boundary layer. Additionally, the profiles for v in Fig. 6b indicate a broader, weaker vortex as compared to the $M_\infty = 0.8$ and $M_\infty = 0.7$ cases.

In progressing through the five downstream locations of Fig. 6, whether for constant J or constant M_∞, it can be seen that the magnitude of v associated with the vortex pair is reduced and its peak moved farther from the wall. This suggests that, as the interaction proceeds farther downstream, the vortex strength ebbs, although strictly speaking, changes in the magnitude of v may result either from changes in the strength of the vortex pair or the distance between them. Additionally, the peak in v becomes wider downstream, suggesting that the vortices grow spatially as their maximum vertical velocity declines. Similarly, the velocity deficit in u can be observed to diminish with downstream distance in Fig. 5, indicating a gradual recovery from the wake effect of the jet.

Figure 6 also shows a small region of negative values of v near the wall for all cases except $J = 2.8$, $M_\infty = 0.6$, and $M_\infty = 0.5$. This

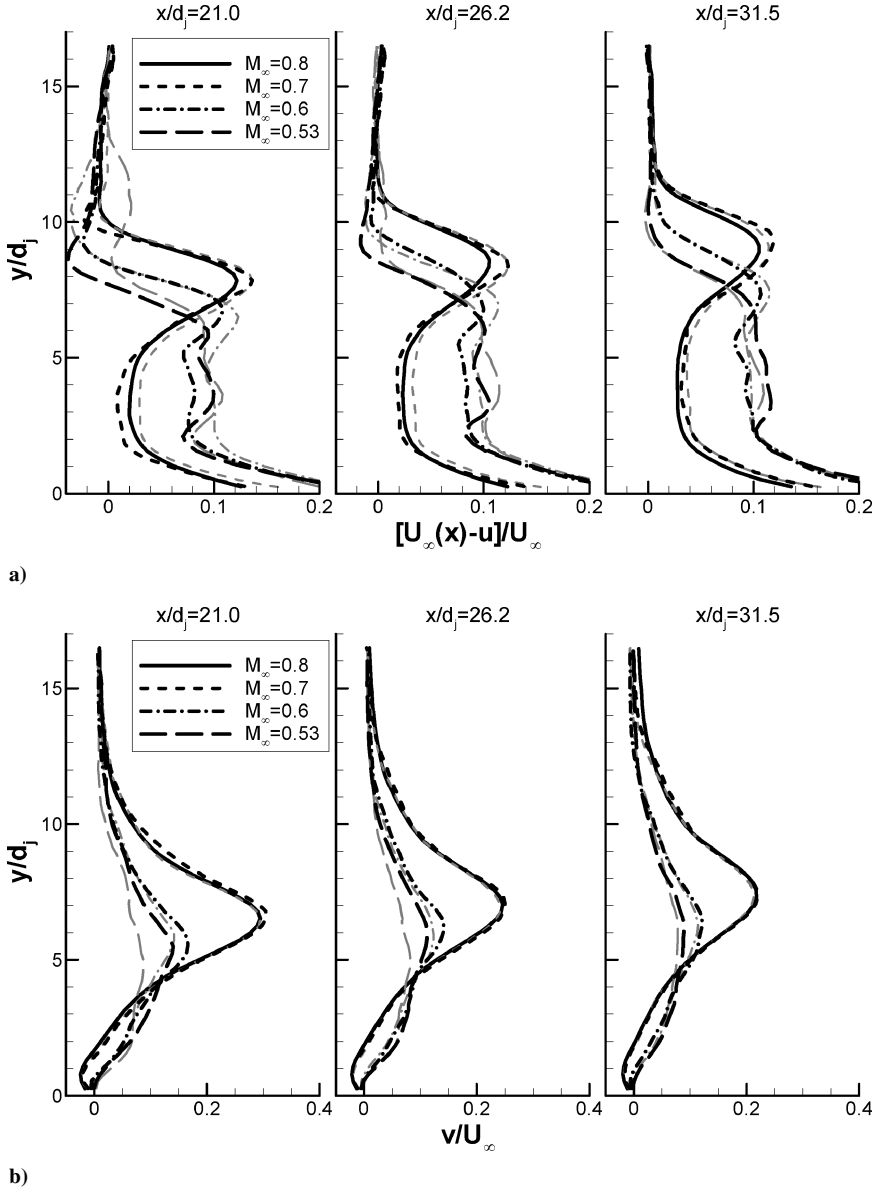

Fig. 7 Mean velocity profiles at three locations downstream of jet nozzle centerline for varying M_∞ while $J = 10.2$; dark lines, data at which Reynolds number is constant and gray lines, data at which static pressure is constant: a) streamwise velocity deficit and b) vertical velocity component.

may indicate the presence of a smaller, weaker vortex rotating in the opposite direction near the wall beneath the primary vortex pair, which would find precedent from the incompressible observations of Haven and Kurosaka[22] and may be due to the downstream remnant of the horseshoe vortices shown in Fig. 1.[11,12]

The lack of J similarity in the $M_\infty = 0.6$ and $M_\infty = 0.5$ data could potentially be explained by Reynolds number differences. At $M_\infty = 0.8$, the wind tunnel unit Reynolds number is 19×10^6 m^{-1} and falls to 16×10^6 m^{-1}, 14×10^6 m^{-1}, and 11×10^6 m^{-1} for $M_\infty = 0.7$, 0.6, and 0.5, respectively, because the static pressure is held constant at 101 kPa. To assess the influence of the Reynolds number, one additional wind-tunnel run was conducted at each of the three lower Mach numbers with $Re = 19 \times 10^6$ m^{-1} by appropriately increasing the tunnel stagnation pressure. The $M_\infty = 0.5$ condition was replaced with $M_\infty = 0.53$ to remain within the operating constraints of the wind tunnel. Data were collected from the upstream imaging location only. Figure 7 shows the resulting velocity data at three downstream locations and compares it with the data from Figs. 5 and 6. Clearly, the Reynolds number has only a secondary effect and cannot explain the apparent interaction between the jet and the boundary layer. It is conceivable that flow separation within the jet nozzle at $M_\infty = 0.6$ and $M_\infty = 0.5$ leads to the subsequent flowfield difference, but this seems unlikely given that similar separation is seen for the $J = 5.6$ and $J = 2.8$ cases[43] without inducing such an interaction.

The failure of the $M_\infty = 0.6$ and $M_\infty = 0.5$ cases to exhibit similarity with the $M_\infty = 0.8$ and $M_\infty = 0.7$ cases is contrary to an earlier experiment within the same research program, in which schlieren images were acquired of the same interaction.[43] Those data showed a qualitatively identical jet penetration for all four values of M_∞ at $J = 10.2$. However, in that study, the nozzle exit diameter was 12.7 mm (0.500 in.), in contrast to the present value of 9.53 mm (0.375 in.); therefore, a different ratio existed for the nozzle exit diameter to the crossflow wall boundary-layer thickness. Past studies have shown this to be a relevant parameter in the development of the jet-in-crossflow interaction,[44–47] and this may be a factor in the differing interaction behavior.

Jet Trajectory and Scaling

Velocity profiles such as those shown in Figs. 5 and 6 were used to compute the trajectory of the jet based on the maximum values of the deficit in u and the v velocity component. At each horizontal position in the mean vector fields, a least-squares fit of a quadratic polynomial was applied to the seven data points encompassing the velocity

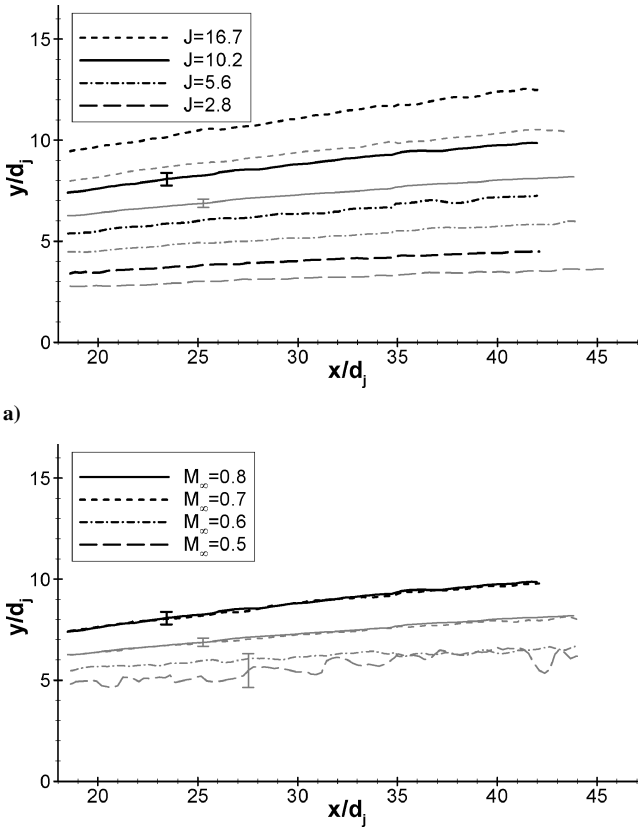

Fig. 8 Jet trajectories found as loci of peak velocity locations; dark lines, trajectories derived from the streamwise velocity deficit and gray lines, trajectories from vertical velocity component: a) varying J while $M_\infty = 0.8$ and b) varying M_∞ while $J = 10.2$.

peak, from which the maximum value and its vertical location were derived at a spatial resolution superior to the PIV measurement volume. A trajectory then was formed from the locus of resulting spatial points. This procedure was performed independently for u and v.

Figure 8 shows the trajectories derived from u and v, which are not identical. This occurs because u reaches a maximum deficit in the jet core and v peaks between the two vortices, which are situated below the jet as shown in Fig. 1. Error bars are provided for the case in which $J = 10.2$ and $M_\infty = 0.8$ by analyzing deviations in the trajectories acquired from wind-tunnel runs conducted on different days using different PIV camera calibrations. These uncertainties are much less than those shown in Figs. 5 and 6 for the velocity profiles because the velocity errors are principally calibration biases and, thus, do not strongly influence the location of the peaks for finding trajectories. The error bars in v for the $J = 10.2$ and $M_\infty = 0.5$ case in Fig. 8b are derived from only a single calibration. In either case, the trajectory error bars principally represent the experimental repeatability and convergence of the mean.

In whichever manner they are found, the trajectories confirm earlier observations. Higher values of J lead to farther penetration of the jet and vortices into the crossflow. The trajectories collapse for $M_\infty = 0.8$ and $M_\infty = 0.7$ when $J = 10.2$, but do not for $M_\infty = 0.6$ and $M_\infty = 0.5$. No trajectories based on u are shown for $M_\infty = 0.6$ and $M_\infty = 0.5$ because no peak velocity deficit is reliably exhibited (as is clear in Fig. 5b). The noisy trajectory found using v for these two cases is directly attributable to the noise seen in Figs. 4f and 4g and falls within the estimated uncertainty.

The jet penetration continues to increase with downstream distance in all cases for the full spatial extent of the present measurements, in contrast with Papamoschou and Hubbard's[19] observation that jet penetration appears to level off at about $x/d_j \approx 6$. The trajectory slope can be seen in Fig. 8a to be greater for larger J.

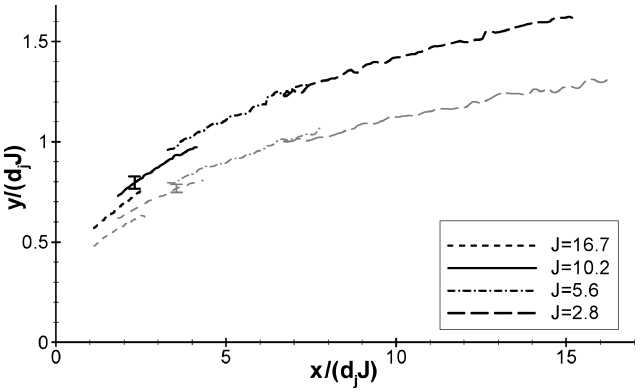

Fig. 9 Jet trajectories where dimensions are additionally normalized by J; dark lines, trajectories derived from streamwise velocity deficit and gray lines, trajectories from vertical velocity component.

Previous studies have indicated that additionally normalizing the dimensions by J can lead to collapse of the jet trajectories into a single curve.[20,30] This is accomplished in Fig. 9, where it appears that such similarity is better at smaller values of J than at large. In comparison, the Gruber et al.[30] similarity was shown only at small J, and although Keffer and Baines found excellent collapse at large J, their experiment was incompressible.[20] It does appear in Fig. 9, however, that the slope of the trajectories blend together smoothly and the discrepancies arise from an offset, which can be seen to exceed the measurement uncertainty. Regardless, the present data confirm that J is an invaluable similarity parameter, but not an exclusive one.

Vortex Size and Strength

The size and strength of the counter-rotating vortex pair may be inferred from the vertical velocity component. Although the vorticity in the crossplane is additionally a function of the lateral velocity (the w component), v alone provides a good measure of the vortex behavior because the laser sheet passes through the nominal centerline of the interaction where the vorticity is dominated by v. Figure 10 shows the maximum value of v found from the quadratic fit described earlier, which is representative of a combination of the vortex strength and the separation between the vortices. It also shows the width of the v velocity profile, produced by the size and separation of the vortex pair, which is calculated as the full-width half-maximum of the profile found normal to the wall. Uncertainties were calculated in the same manner as for Fig. 8.

Figure 10a concisely presents the earlier observation that both the maximum vertical velocity and the breadth of its peak are greater for larger values of J. It also is seen that, as the maximum v decays with downstream distance, the width of the profile grows. These trends suggest direct implications for jet/fin interactions. Although jets with higher dynamic pressure relative to the freestream will locate the vortex center farther from the wall, as seen in Fig. 8a, the influence on fins or other control surfaces may be increased due to the rise in the strength and extent of v, implying a greater prominence of the vortex pair. Similarly, even though the magnitude of v decays with downstream distance, the inferred increase in the vortex size indicates that its influence may be felt over a greater expanse.

Figure 10b again demonstrates similarity for $M_\infty = 0.8$ and $M_\infty = 0.7$ but not for $M_\infty = 0.6$ and $M_\infty = 0.5$. For the latter two cases, a larger crossflow Mach number leads to a stronger v but its extent is smaller. The deviant behavior of the $M_\infty = 0.6$ and $M_\infty = 0.5$ cases exceeds the measurement uncertainty.

Finally, another examination of similarity with J can be made with the vertical velocity measurements. Figure 11 displays the data from Fig. 10b scaled with $d_j J$ rather than simply d_j, analogous to the Fig. 9 treatment of the jet trajectories. The velocity magnitude displays strong similarity and is valid to within the measurement uncertainty, but the profile width clearly cannot be collapsed in this fashion. Previous studies suggest that the vortex width may exhibit

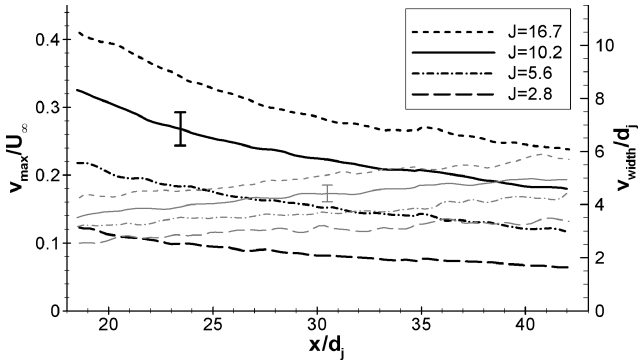

a)

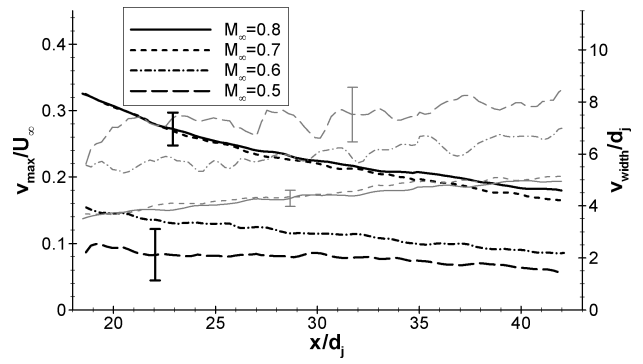

b)

Fig. 10 Magnitude and extent of the vertical velocity component induced by the counter-rotating vortex pair; dark lines, maximum vertical velocity component, shown on the left *y* axis, and gray lines, width of the vertical velocity peak, shown on the right *y* axis: a) varying J while $M_\infty = 0.8$ and b) varying M_∞ while $J = 10.2$.

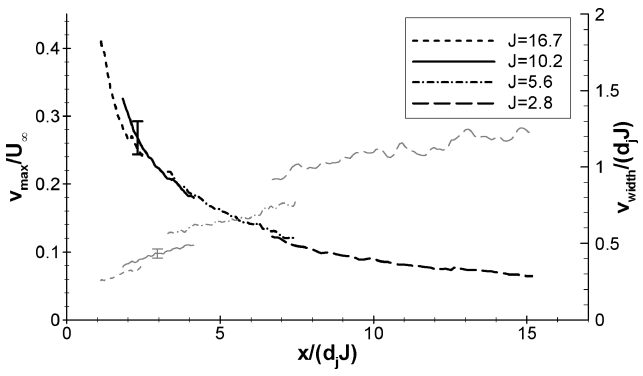

Fig. 11 Magnitude and extent of the vertical velocity component induced by the counter-rotating vortex pair where dimensions are additionally normalized by J; dark lines, vertical velocity maximum on left *y* axis and gray lines, width of peak on right *y* axis.

similarity if it is measured normal to the local trajectory of the jet,[20,23] but at the small trajectory angles of the present far-field measurements, this was found not to have an appreciable effect. The lack of similarity may occur because the vortex width is found exclusively from the v component and neglects the w component.

Summary

PIV data have been acquired in the centerline streamwise plane of the far field of the interaction generated by an overexpanded axisymmetric supersonic jet exhausting transversely from a flat plate into a subsonic compressible crossflow. Mean vector fields were found by averaging at least 1000 individual vector fields for each of seven sets of flowfield conditions varying the jet-to-freestream dynamic pressure ratio J and the crossflow Mach number M_∞. The presence of the decaying jet and the induced counter-rotating vortex pair is evident in both u and v components of velocity (the streamwise and vertical directions, respectively). The velocity deficit in u is found a greater distance from the wall than the increase in v, suggesting that the velocity deficit is caused by the jet itself, which is situated above the vortex pair that generates the increase in v. A smaller velocity deficit also is found between the vortices and the wall due to a wakelike effect of the jet.

In all cases, the peak of the velocity deficit in u and the maximum exhibited in v both move farther from the wall with increasing downstream distance. As the magnitude of the vertical velocity decays, its spatial extent increases. Larger values of J while M_∞ remains constant produce broader profiles of greater vertical velocities as well as a larger streamwise velocity deficit. This indicates that even though stronger jets locate the induced vortex pair farther from the wall, their influence on aerodynamic surfaces such as fins or strakes may be enhanced.

For cases in which $M_\infty = 0.8$ and $M_\infty = 0.7$ while J is constant, similarity in the velocity field is observed. Conversely, at $M_\infty = 0.6$ and $M_\infty = 0.5$ for constant J, different jet trajectories and vortex behavior are observed, which appears to result from an interaction between the jet and the wall boundary layer. In cases where J is varied and $M_\infty = 0.8$, when the spatial dimensions are scaled using both the jet diameter and J, similarity in the jet trajectory and the velocity maximum is observed. However, such collapse is better at lower values of J. Furthermore, no such similarity was found for the vertical velocity profile width.

These measurements of the jet trajectory and the associated velocity magnitudes, coupled with inferences concerning the counter-rotating vortex pair size and location, are useful for understanding the jet penetration properties as pertaining to jet/fin interactions on atmospheric flight vehicles. Additionally, the detailed velocity data offer quantitative measurements for use in validating computational models and developing their predictive capability.

Acknowledgments

The authors thank the following Sandia National Laboratories staff members for their insightful advice and discussions: W. L. Oberkampf, J. L. Payne, C. W. Peterson, M. R. Prairie, and W. P. Wolfe. This work is supported by Sandia National Laboratories and the U.S. Department of Energy. Sandia is a multiprogram laboratory operated by Sandia Corporation, a Lockheed Martin Company, for the U.S. Department of Energy's National Nuclear Security Administration under Contract DE-AC04-94AL85000.

References

[1]Margason, R. J., "Fifty Years of Jet in Cross Flow Research," *Computational and Experimental Assessment of Jets in Cross Flow*, CP-534, AGARD, 1993, pp. 1.1–1.41.

[2]Lee, E. E., Jr., and Willis, C. M., "Interaction Effects of a Control Jet Exhausting Radially from the Nose of an Ogive-Cylinder Body at Transonic Speeds," NASA TN D-3752, Jan. 1967.

[3]Cassel, L. A., Durando, N. A., Bullard, C. W., and Kelso, J. M., "Jet Interaction Control Effectiveness for Subsonic and Supersonic Flight," U.S. Army Missile Command, Rept. RD-TR-69-21, Redstone Arsenal, AL, Sept. 1969.

[4]Manela, J., and Seginer, A., "Interaction of Multiple Supersonic Jets with a Transonic Flowfield," *AIAA Journal*, Vol. 24, No. 3, 1986, pp. 418–423.

[5]Dormieux, M., and Marsaa-Poey, R., "Numerical Assessment of Aerodynamic Interactions on Missiles with Transverse Jets Control," *Computational and Experimental Assessment of Jets in Cross Flow*, CP-534, AGARD, 1993, pp. 30.1–30.11.

[6]Graham, M. J., and Weinacht, P., "Numerical Investigation of Supersonic Jet Interaction for Axisymmetric Bodies," *Journal of Spacecraft and Rockets*, Vol. 37, No. 5, 2000, pp. 675–683.

[7]Cassel, L. A., "Applying Jet Interaction Technology," *Journal of Spacecraft and Rockets*, Vol. 40, No. 4, 2003, pp. 523–537.

[8]Srivastava, B., "Aerodynamic Performance of Supersonic Missile Body- and Wing Tip-Mounted Lateral Jets," *Journal of Spacecraft and Rockets*, Vol. 35, No. 3, 1998, pp. 278–286.

[9]Brandeis, J., and Gill, J., "Experimental Investigation of Super- and Hypersonic Jet Interaction on Missile Configurations," *Journal of Spacecraft and Rockets*, Vol. 35, No. 3, 1998, pp. 296–302.

[10]Graham, M. J., Weinacht, P., and Brandeis, J., "Numerical Investigation of Supersonic Jet Interaction for Finned Bodies," *Journal of Spacecraft and Rockets*, Vol. 39, No. 3, 2002, pp. 376–383.

[11]Fric, T. F., and Roshko, A., "Vortical Structure in the Wake of a Transverse Jet," *Journal of Fluid Mechanics*, Vol. 279, 1994, pp. 1–47.

[12]Krothapalli, A., Lourenco, L., and Buchlin, J. M., "Separated Flow Upstream of a Jet in a Crossflow," *AIAA Journal*, Vol. 28, No. 3, 1990, pp. 414–420.

[13]Kelso, R. M., and Smits, A. J., "Horseshoe Vortex Systems Resulting from the Interaction between a Laminar Boundary Layer and a Transverse Jet," *Physics of Fluids*, Vol. 7, No. 1, 1995, pp. 153–158.

[14]Kelso, R. M., Lim, T. T., and Perry, A. E., "An Experimental Study of Round Jets in Cross-Flow," *Journal of Fluid Mechanics*, Vol. 306, 1996, pp. 111–144.

[15]Sykes, R. I., Lewellen, W. S., and Parker, S. F., "On the Vorticity Dynamics of a Turbulent Jet in a Crossflow," *Journal of Fluid Mechanics*, Vol. 168, 1986, pp. 393–413.

[16]Yuan, L. L., Street, R. L., and Ferziger, J. H., "Large-Eddy Simulations of a Round Jet in Crossflow," *Journal of Fluid Mechanics*, Vol. 379, 1999, pp. 71–104.

[17]Orth, R. C., and Funk, J. A., "An Experimental and Comparative Study of Jet Penetration in Supersonic Flow," *Journal of Spacecraft*, Vol. 4, No. 9, 1967, pp. 1236–1242.

[18]Kamotani, Y., and Greber, I., "Experiments on a Turbulent Jet in a Crossflow," *AIAA Journal*, Vol. 10, No. 11, 1972, pp. 1425–1429.

[19]Papamoschou, D., and Hubbard, D. G., "Visual Observations of Supersonic Transverse Jets," *Experiments in Fluids*, Vol. 14, No. 6, 1993, pp. 468–471.

[20]Keffer, J. F., and Baines, W. D., "The Round Turbulent Jet in a Cross-Wind," *Journal of Fluid Mechanics*, Vol. 15, 1963, pp. 481–496.

[21]Andreopoulos, J., and Rodi, W., "Experimental Investigation of Jets in a Crossflow," *Journal of Fluid Mechanics*, Vol. 138, 1984, pp. 93–127.

[22]Haven, B. A., and Kurosaka, M., "Kidney and Anti-Kidney Vortices in Crossflow Jets," *Journal of Fluid Mechanics*, Vol. 352, 1997, pp. 27–64.

[23]Hasselbrink, E. F., Jr., and Mungal, M. G.., "Transverse Jets and Jet Flames. Part 2. Velocity and OH Field Imaging," *Journal of Fluid Mechanics*, Vol. 443, 2001, pp. 27–68.

[24]Kim, K. C., and Park, K. Y., "Evolution of the Counter-Rotating Vortex Structure in a Crossflow Jet," *JSME International Journal*, Series B, Vol. 43, No. 4, 2000, pp. 659–664.

[25]Meyer, K. E., Ozcan, O., and Westergaard, C. H., "Flow Mapping of a Jet in Crossflow with Stereoscopic PIV," *Journal of Visualization*, Vol. 5, No. 3, 2002, pp. 225–231.

[26]Santiago, J. G., and Dutton, J. C., "Velocity Measurements of a Jet Injected into a Supersonic Crossflow," *Journal of Propulsion and Power*, Vol. 13, No. 2, 1997, pp. 264–273.

[27]McCann, G. J., and Bowersox, R. D. W., "Experimental Investigation of Supersonic Gaseous Injection into a Supersonic Freestream," *AIAA Journal*, Vol. 34, No. 2, 1996, pp. 317–323.

[28]Mahmud, Z., and Bowersox, R., "Supersonic Missile Body Jet Interaction Flowfields at Low Momentum-Parameter-Ratio," AIAA Paper 2003-1244, Jan. 2003.

[29]Fuller, E. J., Mays, R. B., Thomas, R. H., and Schetz, J. A., "Mixing Studies of Helium in Air at High Supersonic Speeds," *AIAA Journal*, Vol. 30, No. 9, 1992, pp. 2234–2243.

[30]Gruber, M. R., Nejad, A. S., Chen, T. H., and Dutton, J. C., "Mixing and Penetration Studies of Sonic Jets in a Mach 2 Freestream," *Journal of Propulsion and Power*, Vol. 11, No. 2, 1995, pp. 315–323.

[31]Kraus, D. K., and Cutler, A. D., "Mixing of Swirling Jets in a Supersonic Duct Flow," *Journal of Propulsion and Power*, Vol. 12, No. 1, 1996, pp. 170–177.

[32]McDaniel, J. C., and Graves, J., Jr., "Laser-Induced-Fluorescence Visualization of Transverse Gaseous Injection in a Nonreacting Supersonic Combustor," *Journal of Propulsion*, Vol. 4, No. 6, 1988, pp. 591–597.

[33]Dahlke, C. W., "An Experimental Investigation of Downstream Flowfield Properties Behind a Forward Located Sonic Jet Injected into Transonic Freestream from a Body of Revolution," U.S. Army Missile Command, Rept. RD-TM-68-2, Redstone Arsenal, AL, Jan. 1968.

[34]Chocinski, D., and Leblanc, R., "Experimental/Computational Investigation of Supersonic Jet in Subsonic Compressible Crossflow," AIAA Paper 97-0714, Jan. 1997.

[35]Prasad, A. K., and Adrian, R. J., "Stereoscopic Particle Image Velocimetry Applied to Liquid Flows," *Experiments in Fluids*, Vol. 15, No. 1, 1993, pp. 49–60.

[36]Yoon, J. H., and Lee, S. J., "Direct Comparison of 2D PIV and Stereoscopic PIV Measurements," *Measurement Science and Technology*, Vol. 13, No. 10, 2002, pp. 1631–1642.

[37]Samimy, M., and Lele, S. K., "Motion of Particles with Inertia in a Compressible Free Shear Layer," *Physics of Fluids A*, Vol. 3, No. 8, 1991, pp. 1915–1923.

[38]Melling, A., "Tracer Particles and Seeding for Particle Image Velocimetry," *Measurement Science and Technology*, Vol. 8, No. 12, 1997, pp. 1406–1416.

[39]Adrian, R. J., "Scattering Particle Characteristics and Their Effect on Pulsed Laser Measurements of Fluid Flow: Speckle Velocimetry vs. Particle Image Velocimetry," *Applied Optics*, Vol. 23, No. 11, 1984, pp. 1690–1691.

[40]Meynart, R., "Non-Gaussian Statistics of Speckle Noise of Young's Fringes in Speckle Velocimetry," *Applied Optics*, Vol. 24, No. 10, 1985, pp. 1448–1453.

[41]Westerweel, J., Dabiri, D., and Gharib, M., "The Effect of a Discrete Window Offset on the Accuracy of Cross-Correlation Analysis of Digital PIV Recordings," *Experiments in Fluids*, Vol. 23, No. 1, 1997, pp. 20–28.

[42]Beresh, S. J., Amatucci, V. A., Henfling, J. F., Erven, R. J., and Bourdon, C. J., "Pressure Measurements Onboard a Small-Scale Rotating Wind Tunnel Model for Jet/Fin Interaction," AIAA Paper 2002-3137, June 2002.

[43]Beresh, S. J., Henfling, J. F., and Erven, R. J., "Flow Separation Inside a Supersonic Nozzle Exhausting into a Subsonic Compressible Crossflow," *Journal of Propulsion and Power*, Vol. 19, No. 4, 2003, pp. 655–662.

[44]Schetz, J. A., and Billig, F. S., "Penetration of Gaseous Jets Injected into a Supersonic Stream," *Journal of Spacecraft and Rockets*, Vol. 3, No. 11, 1966, pp. 1658–1665.

[45]Gruber, M. R., Nejad, A. S., Chen, T. H., and Dutton, J. C., "Compressibility Effects in Supersonic Transverse Injection Flowfields," *Physics of Fluids*, Vol. 9, No. 5, 1997, pp. 1448–1461.

[46]Roger, R. P., and Chan, S. C., "Parameters Affecting Penetration of a Single Jet into a Supersonic Crossflow: A CFD Study—II," AIAA Paper 98-0425, Jan. 1998.

[47]Cortelezzi, L., and Karagozian, A. R., "On the Formation of the Counter-Rotating Vortex Pair in Transverse Jets," *Journal of Fluid Mechanics*, Vol. 446, 2001, pp. 347–373.

R. Lucht
Associate Editor